Bistable spiral wave dynamics in electrically excitable media

Zhaoyang Zhang,[1,*] Yuhao Zhang,[1] and Zhilin Qu[2,†]
[1]*Department of Physics, School of Physical Science and Technology, Ningbo University, Ningbo, Zhejiang 315211, China*
[2]*Department of Medicine, David Geffen School of Medicine, University of California, Los Angeles, California 90095, USA*

(Received 1 September 2023; accepted 13 November 2023; published 8 December 2023)

We show that a positive feedback loop between sodium current inactivation and wave-front ramp-up speed causes a saddle-node bifurcation to result in bistable planar and spiral waves in electrically excitable media, in which both slow and fast waves are triggered by different stimulation protocols. Moreover, the two types of spiral wave conduction may interact to give rise to more complex spiral wave dynamics. The transitions between different spiral wave behaviors via saddle-node bifurcation can be a candidate mechanism for transitions widely seen in cardiac arrhythmias and neural diseases.

DOI: 10.1103/PhysRevE.108.064405

I. INTRODUCTION

Spiral wave is a ubiquitous phenomenon in nature [1,2], including chemical reactions [3–5], slime mold [6–8], intracellular calcium signaling [9,10], brain waves [11,12], and abnormal electrical activity in the heart [13,14], etc. A rich spectrum of spiral wave dynamics has been shown [15–20], including stable spiral waves, meandering spiral waves, and spiral wave breakup. These spiral wave dynamics result in periodic, quasiperiodic, and chaotic behaviors. In addition to these rich spiral wave dynamics, another nonlinear dynamical behavior of spiral wave has been shown in excitable media, i.e., bistability in spiral wave conduction. Bistable spiral wave behavior was shown in an early study by Winfree [21] in an excitable medium with the FitzHugh-Nagumo (FHN) model, in which two types of stable spiral waves, a fast one and a slow one, can occur in the same medium and the spiral wave period exhibits a hysteresis of a typical bistable system. Similar bistable spiral wave behavior was also shown in a coupled map model in an early theoretical study by Ito and Glass [22]. In a more recent study by Zykov and Bodenschatz [23], the authors showed that bistable spiral wave could occur when the FHN-type model is near or in bistability. Similarly, bistable conduction in a cable was shown when the FHN model is near or in bistability [24]. So far, no experimental evidence has been shown in generic excitable media to support the bistable spiral wave dynamics. In previous studies [25,26], we showed in computer simulations and experiments that another type of bistable spiral wave behavior can occur in cardiac tissue. In this type of bistable behavior, L-type calcium (Ca^{2+}) current ($I_{Ca,L}$)-mediated slow spiral wave and sodium (Na^{+}) current (I_{Na})-mediated fast spiral wave can occur in the same tissue. In this case, early afterdepolarizations are needed and the resting potentials for the two types of spiral wave are different: one is around −80 mV and the other is around −40 mV. Early afterdepolarizations are secondary depolarizations in the plateau phase of the action potential, which are a hallmark of long QT syndrome [27]. In these previous studies [25,26], experimental evidence of bistable reentry was shown in cultured ventricular myocyte monolayers, supporting the simulation results.

Theoretical analyses have shown that wave-front conduction in excitable media exhibits a stable fast conduction and an unstable slow conduction [28,29]. In other words, in general, excitable media exhibit a single stable conduction. In a recent study [30], we showed an interesting conduction behavior in nerve cables or fibers in which stable slow and fast conduction occur under the same condition, namely a bistable conduction. This behavior is promoted by altering the I_{Na} kinetics, namely by speeding up I_{Na} inactivation. The underlying mechanism is that the positive feedback loop between I_{Na} inactivation and the ramp-up speed of the wave front results in two ramp-up speeds (or two inactivation modes) during conduction in the cable. This theory provides a mechanism for the experimental observations of fast and slow conduction in the giant axons of jellyfish [31] and cockroaches [32]. Moreover, this bistable conduction theory unifies the seemingly contradictory experimental observations under a single theoretical framework [30]. Inspired by this study, we hypothesize that since the bistable conduction is promoted by only altering the I_{Na} inactivation kinetics, it may be applicable to other electrically excitable media, such as cardiac fibers and tissue. Moreover, this same bistable planar wave conduction mechanism in cable may lead to bistable spiral waves in tissue, including both cardiac and neural tissue. In this study, we use numerical simulation to investigate bistable conduction and spiral wave dynamics in cardiac and neural tissue models under the condition of altered I_{Na} inactivation kinetics.

II. METHODS

We carry out simulations in both one-dimensional (1D) cable and two-dimensional (2D) tissue using both cardiac and neural action potential models. The governing equation of voltage (V) for a 1D cable is

$$\frac{\partial V}{\partial t} = -\frac{I_{ion} + I_{sti}}{C_m} + D\frac{\partial^2 V}{\partial x^2} \tag{1}$$

*zhangchaoyang@nbu.edu.cn
†zqu@mednet.ucla.edu

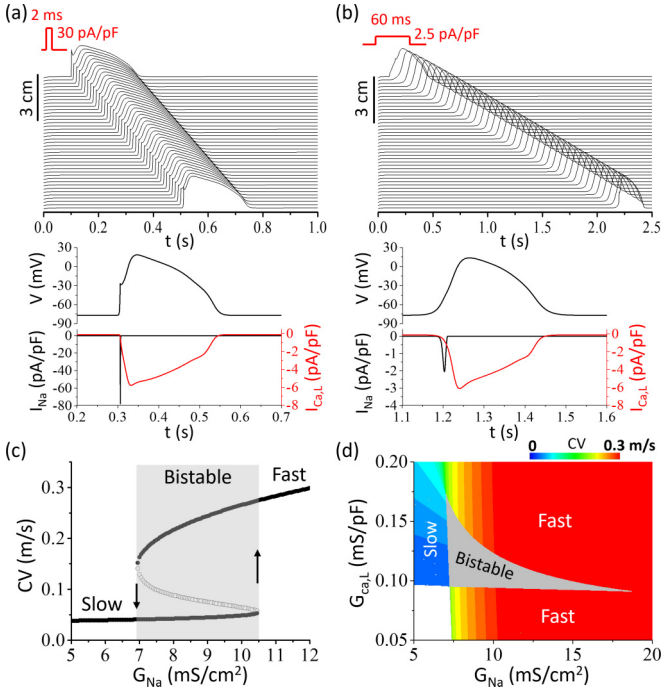

FIG. 1. Bistable conduction in a cardiac fiber. (a) Space-time plot of V showing a fast wave in a 9-cm cable triggered by a strong but short square pulse (as indicated on top). The panels below show recording of V, I_{Na}, and $I_{Ca,L}$ versus time from the middle of the cable. (b) Space-time plot of V showing a slow wave in the same cable triggered by a weak but long square pulse (as indicated on top). The panels below show recording of V, I_{Na}, and $I_{Ca,L}$ versus time from the middle of the cable. (c) Hysteresis showing CV versus G_{Na} in the same cable as in (a) and (b). Gray background is the G_{Na} range for bistable conduction. (d) Phase diagram showing conduction behaviors in the G_{Na} and $G_{Ca,L}$ plane. The gray region is bistable conduction. The phase diagram is obtained using the strong and weak stimulation protocols as in (a) and (b). $G_{Na} = 9$ mS/cm^2 is used for panels (a) and (b).

and for 2D tissue is

$$\frac{\partial V}{\partial t} = -\frac{I_{ion} + I_{sti}}{C_m} + D\left(\frac{\partial^2 V}{\partial x^2} + \frac{\partial^2 V}{\partial y^2}\right). \tag{2}$$

In Eqs. (1) and (2), $C_m = 1$ μF/cm^2 is the membrane capacitance, I_{ion} is the total ionic current density and I_{sti} is the stimulation current density, which is a square pulse. $D = 0.0005$ cm^2/ms is the diffusion constant. The specific functional form of I_{ion} and the differential equations of other variables are different in different action potential models. Most of the results in this study are obtained using the 1991 Luo and Rudy (traditionally labeled as the LR1) model [33], and the major conclusions are also demonstrated using physiologically more detailed action potential models [34–36] and a modified Hodgkin-Huxley (HH) neural action potential model [30]. A strong and narrow I_{sti} is used to induce a fast wave, and a weak and wide I_{sti} is used to induce a slow wave in the 1D cable [see Figs. 1(a) and 1(b)]. The traditional cross-field stimulation protocol is used for spiral wave induction in 2D tissue. Similar to the 1D cable, a strong and narrow I_{sti} is used for initiating a fast spiral wave and a weak and wide I_{sti} is used for initiating a slow spiral wave. Computer simulations are carried out using a forward Euler method for Eqs. (1) and (2) with $\Delta x = \Delta y = 0.015$ cm and $\Delta t = 0.01$ ms. Graphic processing unit computation with CUDA programming is used for simulations. No flux boundary conditions are used.

III. RESULTS

We first carry out 1D cable simulations to investigate if the bistable conduction that we have shown in nerve fibers previously [30] can still occur in cardiac fibers. Figure 1 shows the 1D cable simulation results using the LR1 model with parameter alterations (see the Appendix). Although changes of several parameters are needed to maintain certain properties, such as the action potential duration, the common changes required for bistable conduction are reduction of the inactivation time constant (τ_h) and the maximum conduction (G_{K1}) of I_{K1}. Figures 1(a) and 1(b) show a fast-conducting wave and a slow-conducting wave in the same cable initiated with two different stimuli, respectively. The fast wave is induced by a short square pulse with a high amplitude [Fig. 1(a)], and the slow wave is induced by a long square pulse with a low amplitude [Fig. 1(b)]. It takes about 400 ms for the fast wave but more than 2 s for the slow wave to conduct from one end to the other end of the 9-cm cable. The two distinct conduction dynamics are due to two different modes of I_{Na} strength. In the fast wave, the voltage ramps up quickly with a high I_{Na} (≈ -80 pA/pF). In the slow wave, the voltage ramps up much more slowly with a low I_{Na} (≈ -2 pA/pF). As we showed previously [30], the two modes of I_{Na} are due to two modes of inactivation promoted by the positive feedback between I_{Na} inactivation and wave-front ramp-up speed. In both cases, $I_{Ca,L}$ are almost the same (≈ -6 pA/pF). One can calculate both the stable and unstable conduction velocity (CV) for different G_{Na}, which forms a typical hysteresis with saddle-node bifurcations [Fig. 1(c)] as seen in generic bistable systems. When G_{Na} is small, only slow conduction exists independent of the stimulation protocol. When G_{Na} is large, only fast conduction exists, which is also independent of the stimulation protocol. In the middle range of G_{Na} (gray regime), however, both fast and slow conduction exist, and which type of conduction occurs depends on the stimulation protocol. The unstable CV (open circles) is calculated by using the same protocol as detailed in our previous study [30]. To show how the bistable conduction is affected by I_{Na} and $I_{Ca,L}$, we scan the maximum conductance of I_{Na} (G_{Na}) and that of $I_{Ca,L}$ ($G_{Ca,L}$), and plot CV in color in the two-parameter plane [Fig. 1(d)]. The gray region in Fig. 1(d) is where bistable conduction occurs. The white region is where both stimuli fail to elicit conduction (conduction failure). The colored regions are where both stimuli give rise to a single stable conduction with CV color coded. Bistable conduction occurs in the intermediate range of $G_{Ca,L}$. The mechanism of the bistable conduction is the same as the one in nerve conduction shown in our previous study [30]. Namely, the voltage ramp-up speed and I_{Na} inactivation form a positive feedback loop during conduction, i.e., a faster upstroke causes less inactivation of I_{Na} (and thus a larger I_{Na}), which in turn causes an even faster upstroke. This positive feedback causes bistable conduction

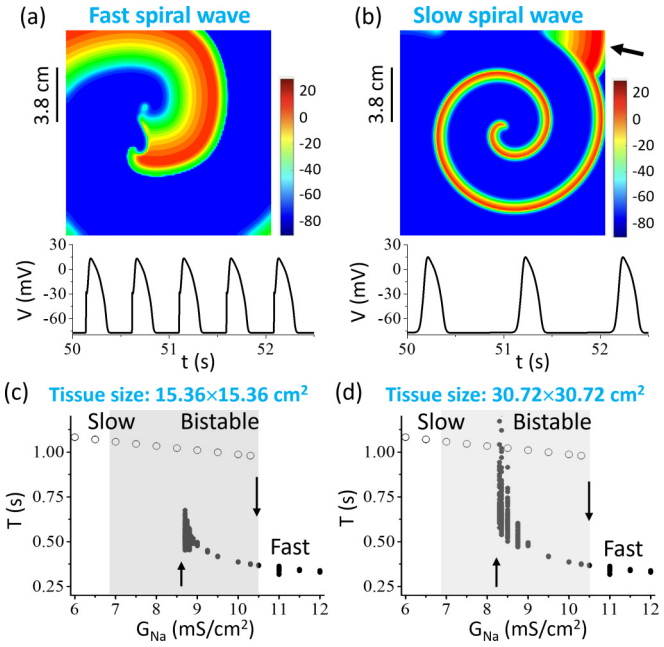

FIG. 2. Bistable spiral wave dynamics in 2D tissue. (a) Upper (Video 1 [37]): A voltage snapshot of the fast spiral wave. Lower: Voltage versus t recorded from a point in the tissue. (b) Upper (Video 2): A voltage snapshot of the slow spiral wave. Lower: Voltage versus t recorded from a point in the tissue. (c) T versus G_{Na} for a tissue size of $15.36 \times 15.36\,\mathrm{cm}^2$. Gray color is the G_{Na} range of bistable conduction in the 1D cable shown in Fig. 1(c). The down arrow indicates the transition point from slow to fast spiral wave as G_{Na} increases. The up arrow indicates the transition point from fast to slow spiral wave as G_{Na} decreases. (d) Same as (c) but for a tissue size of $30.72 \times 30.72\,\mathrm{cm}^2$. The parameters for the action potential model are the same as for Fig. 1. $G_{\mathrm{Na}} = 9\ \mathrm{mS/cm}^2$ is used for panels (a) and (b). In (c) and (d), for each G_{Na} a strong stimulus and a weak stimulus are used to initiate spiral waves. The strong stimulus gives rise to a fast spiral wave and the weak one gives rise to a slow spiral wave in the bistable regime (between the two arrows) but both give rise to a single type of spiral waves (either a fast or a slow wave) outside the bistable regime. The period T is recorded from a point in the spiral arm, e.g., the center of the upper-right quadrant of the 2D tissue.

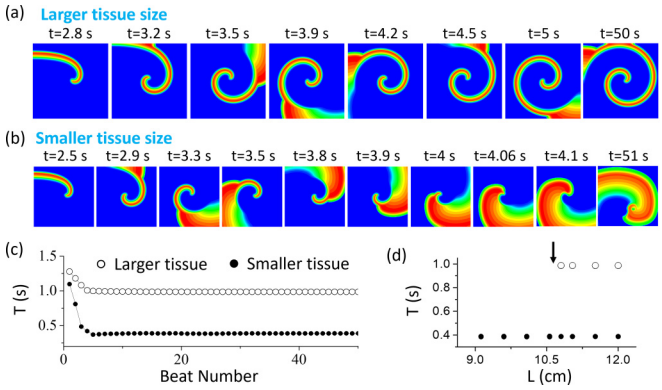

FIG. 3. Tissue size-dependent bistability. (a) Voltage snapshots showing that an initiated slow wave remains as a stable slow wave in a larger tissue (Video 3): $11.52 \times 11.52\,\mathrm{cm}^2$. (b) Voltage snapshots showing that an initiated slow wave degenerates into a fast wave in a smaller tissue (Video 4): $9.6 \times 9.6\,\mathrm{cm}^2$. (c) T versus beat number for the two cases in (a) and (b). (d) T versus tissue size L. For each L, a strong stimulus and a weak stimulus are used to initiate spiral waves, and bistable spiral wave behavior occurs when L is larger than a critical value (arrow). $G_{\mathrm{Na}} = 10\ \mathrm{mS/cm}^2$ is used for all simulations.

to occur. A detailed theoretical analysis in nerve fibers was presented in our previous study [30].

The conduction in a 1D cable corresponds to a planar wave in 2D tissue, and now the questions are whether one can observe bistable spiral waves in 2D tissue and what new dynamics may occur if bistable spiral waves occur. We use the traditional cross-field stimulation protocol to initiate spiral waves in 2D tissue, in which fast and slow spiral waves are induced using different strength stimuli, similar to the ones used in the 1D cable. Indeed, we can observe two types of spiral waves: a fatty-looking fast rotating one [Fig. 2(a); see Supplemental Material Video 1 [37]] and a slim-looking slow rotating one [Fig. 2(b); Video 2]. The period (T) of the fast spiral wave is around 500 ms, and that of the slow one is around 1 s. Similar to the 1D cable, the action potential upstroke of the fast wave is steep and that of the slow wave is much less steep. The action potential durations are similar and the slimness of the slow wave is due to a slower conduction that results in a shorter wavelength. We carry out simulations by scanning G_{Na} to observe hysteresis of spiral wave dynamics. Figure 2(c) shows the spiral wave period T versus G_{Na} in a $15.36 \times 15.36\,\mathrm{cm}^2$ tissue. The bistable conduction region in the 1D cable shown in Fig. 1(c) is painted gray. Note that in Fig. 1(c), the y axis is CV, while in Fig. 2(c), the y axis is T so that the hysteresis is inverted. The transition from the slow spiral wave to the fast spiral wave (down arrow) occurs at roughly the same G_{Na} ($\approx 10.5\ \mathrm{mS/cm}^2$) as for the transition from slow to fast conduction in the 1D cable [up arrow in Fig. 1(c)]. However, the transition from fast to slow spiral wave (up arrow) occurs at a much larger G_{Na} ($\approx 8.6\ \mathrm{mS/cm}^2$) than that ($\approx 7\ \mathrm{mS/cm}^2$) in the 1D cable [down arrow in Fig. 1(c)]. This transition also depends on tissue size, i.e., a smaller G_{Na} is needed in a larger tissue [Fig. 2(d)]. It has been shown that the period T of a spiral wave is determined by the wave-front curvature and CV restitution [18]. Normally, the presence of CV restitution indicates that conduction becomes slower (or weaker) for a shorter period T due to incomplete recovery of I_{Na} [38]. The curvature and CV restitution weaken the fast conduction due to a shorter rotation period T, causing the fast to slow spiral wave transition to occur at a larger G_{Na} than in the 1D cable. Moreover, close to this transition, the period T of the fast spiral wave varies in a wide range and becomes wider as G_{Na} decreases. This is caused by chaotic meander of the spiral wave promoted by the interaction of the two conduction modes, which is discussed in detail later.

The occurrence of bistable spiral wave depends on tissue size. Figure 3 shows spiral wave behaviors in tissues with different sizes. The G_{Na} value ($G_{\mathrm{Na}} = 10\ \mathrm{mS/cm}^2$) is in the middle of the bistable regime [see Figs. 2(c) and 2(d)]. Both spiral waves are initiated as slow waves using the same stimulation protocol (note that if they are initiated as fast waves, they will both remain as stable fast waves in both tissue). For the larger tissue [$11.52 \times 11.52\,\mathrm{cm}^2$; Fig. 3(a) and

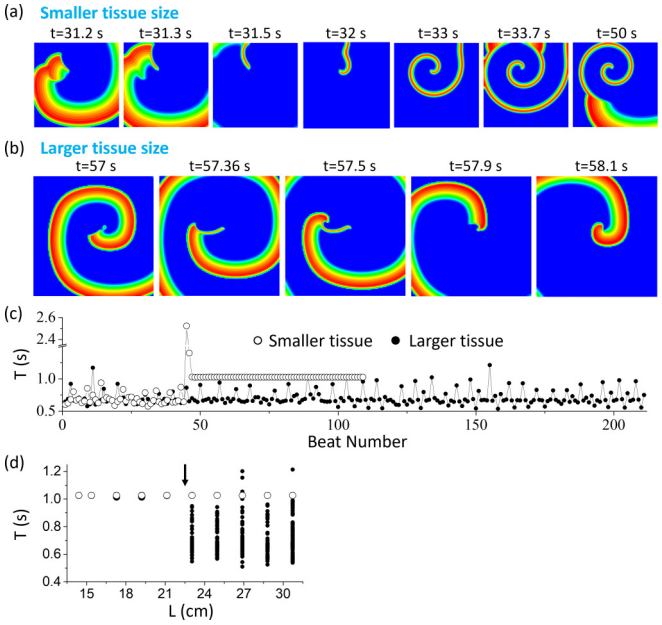

FIG. 4. Tissue size-dependent spiral wave dynamics at the transition from fast to slow wave. (a) Voltage snapshots showing that an initiated fast wave degenerates into a stable slow wave in a smaller tissue (Video 5): $15.36 \times 15.36\,\mathrm{cm}^2$. (b) Voltage snapshots showing an initiated fast wave remains as an intermittent state of fast and slow rotations in a larger tissue (Video 6): $30.72 \times 30.72\,\mathrm{cm}^2$. (c) T versus beat number for the two cases. (d). T versus tissue size L. For each L, a strong stimulus and a weak stimulus are used to initiate spiral waves, and two types of spiral wave behavior occur when L is larger than a critical value (arrow). $G_{\mathrm{Na}} = 8.3\ \mathrm{mS/cm}^2$ is used for all simulations.

Video 3], the slow spiral wave is stable, but for the smaller tissue [$9.6 \times 9.6\,\mathrm{cm}^2$; Fig. 3(b) and Video 4], the slow wave degenerates into the fast wave after only two rotations [see black dots in Fig. 3(c)]. This behavior can be understood as follows. Note that due to the boundary effect, there is a fatty tail in the slow spiral wave [arrow in Fig. 2(b)] which is a fast conduction due to the boundary effect. When the tissue is large enough, the fatty tail constantly emerges and disappears at the tissue boundary without affecting the spiral wave, and thus the spiral wave remains stable as a slow wave [see the open dots in Fig. 3(c)]. When the tissue is small, the fatty tail chases up the slow spiral tip and takes over to result in the fast spiral wave. Therefore, when the tissue is large enough, both fast and slow spiral waves can be observed and the system is bistable, otherwise, only the fast spiral wave can be observed, and the system becomes monostable. Figure 3(d) plots T versus tissue size L, showing that when $L \leqslant 10.6$ cm, only fast waves can be observed, but when $L > 10.6$ cm, both fast and slow waves can be observed.

As shown in Figs. 2(c) and 2(d), the transition from fast to slow spiral wave also depends on tissue size, and at the transition, the fast spiral wave is not stable but meanders to result in a variation in T. To understand these behaviors, we carry out simulations at the transition ($G_{\mathrm{Na}} = 8.3\ \mathrm{mS/cm}^2$) using two tissue sizes [Figs. 4(a) and 4(b)]. In both cases, the spiral waves are initiated as fast waves using the same stimulation protocol (note that if they are initiated as slow waves, they will both remain as stable slow waves). For the smaller tissue [$15.36 \times 15.36\,\mathrm{cm}^2$; Fig. 4(a) and Video 5], the spiral wave meanders with T varying chaotically, which suddenly degenerates into a stable slow wave after $t = 31.5$ s [see open dots in Fig. 4(c)]. However, in the larger tissue [$30.72 \times 30.72\,\mathrm{cm}^2$; Fig. 4(b) and Video 6], this chaotic behavior persists [see black dots in Fig. 4(c)]. Figure 4(d) plots T versus tissue size L, showing that when $L < 22.5$ cm, only stable slow waves can be observed, but when $L > 22.5$ cm, both stable slow and chaotic waves can be observed.

The chaotic meander of the spiral wave is caused by the interaction of the fast and slow conduction in the spiral tip region. As shown in Fig. 4(b), the spiral arm always remains as fast conduction, but in the tip region, frequent transitions between slow and fast conduction occur. Once the spiral tip is a fast conduction, it may degenerate into a slow conduction due to CV restitution and curvature at the spiral tip. Once a slow conduction forms, the fast conduction will chase up and take over. This process repeats to result in the chaotic meandering behavior. However, as the tissue size becomes smaller [such as Fig. 4(a)], the fast spiral arm may disappear at the tissue boundary at some time point, leaving only the slow conduction and thus the slow spiral wave in the tissue. Therefore, if the tissue is not large enough, it can only support the slow wave, causing the transition to occur at a larger G_{Na} in a smaller tissue.

Note that as shown in Figs. 2(c) and 2(d), the variation in T increases as G_{Na} decreases. This is because as G_{Na} reduces, it becomes easier for CV restitution and curvature to convert fast conduction into slow conduction, potentiating this type of fast and slow conduction interaction. Because of the restitution and curvature effect, it requires a larger G_{Na} for the fast to slow transition to occur than that in planar wave in a 1D cable.

To show that this bistable spiral wave dynamics is generic in cardiac tissue, we carry out simulations using physiologically more detailed action potential models, namely, the 1994 Luo and Rudy (LRd) guinea pig ventricular model [34], the 2004 ten Tusscher *et al.* (TP04) human ventricular model [35], and the O'Hara *et al.* (ORd) human ventricular model [36]. These models include more realistic ionic currents and intracellular ion dynamics. The parameters (see the Appendix) are altered to achieve bistability. Although changes of parameters are different for different models to result in bistability, the common changes required are reduction of the inactivation time constant (τ_h) and the maximum conduction (G_{K1}) of I_{K1}. After the parameter changes, we can observe bistable spiral waves for all three models [Figs. 5(a)–5(c)], but spiral waves behave differently in different models. For the LRd model, both fast and slow spiral waves are stable [Fig. 5(a) and Videos 7 and 8], with period $T = 330$ ms and $T = 600$ ms, respectively. For the TP04 model [Fig. 5(b) and Videos 9 and 10], the slow spiral wave is always stable ($T \approx 960$ ms), but the fast spiral wave ($T \approx 540$ ms) suddenly degenerates into the slow wave at around 20 s (Video 9). Figure 5(d) plots a pseudo-electrocardiogram (ECG) (calculated using the standard formulation [39]) to show this transition. The transition is caused by the slow change of intracellular Na^+ concentration ($[Na^+]_i$) (right panel). For the ORd model, the fast spiral wave is not stable but spiral wave breakup exhibiting

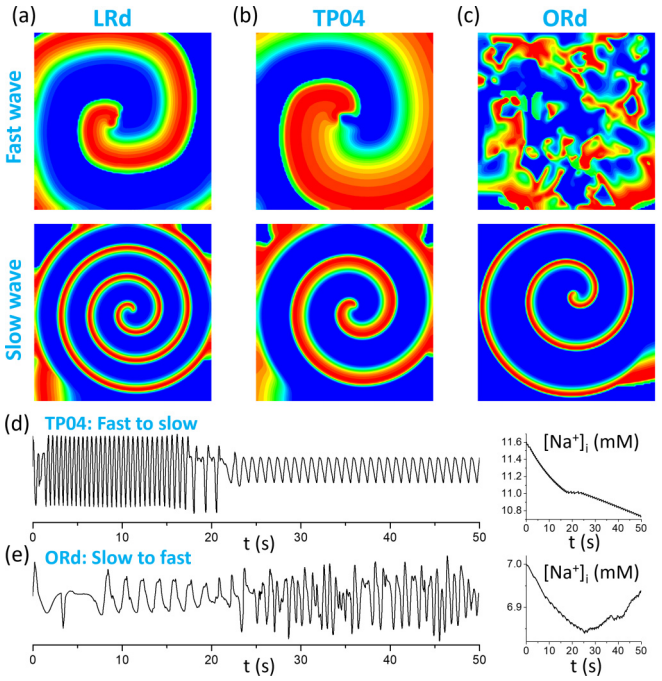

FIG. 5. Bistable spiral wave dynamics in physiologically detailed action potential models. (a)–(c) Voltage snapshots for fast (upper) and slow (lower) spiral waves in 2D tissue with the LRd model [panel (a) and Videos 7 and 8], the TP04 model [panel (b) and Videos 9 and 10], and the ORd model [panel (c) and Videos 11 and 12]. The tissue sizes are $15.36 \times 15.36\,\mathrm{cm}^2$ for the LRd and TP04 model, and $30.72 \times 30.72\,\mathrm{cm}^2$ for the ORd model. (d) Left: Pseudo-ECG showing the spontaneous transition from fast to slow spiral wave for the TP04 model. Right: $[\mathrm{Na}^+]_\mathrm{i}$ versus time from a cell in the tissue. (e) Left: Pseudo-ECG showing the spontaneous transition from a slow spiral wave to spiral wave breakup for the ORd model. Right: $[\mathrm{Na}^+]_\mathrm{i}$ versus time from a cell in the tissue.

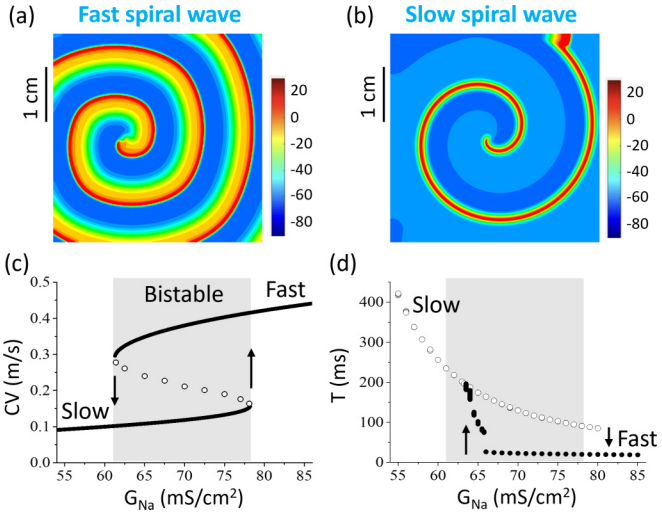

FIG. 6. Bistable planar and spiral wave dynamics in tissue of a modified HH model. (a) Voltage snapshot of the fast spiral wave (Video 13). (b) Voltage snapshot of the slow spiral wave (Video 14). (c) Hysteresis showing CV versus G_Na from a 1D cable. (d) T versus G_Na for spiral waves in 2D tissue. Gray color is the G_Na range [the same as in (c)] of bistable conduction in the 1D cable. Tissue size is $3.84 \times 3.84\,\mathrm{cm}^2$.

spatiotemporal chaos occurs [upper panel in Fig. 5(c) and Video 11]. However, the slow spiral wave is initially stable but suddenly degenerates into the fast spiral wave breakup state at around 20 s in the simulation (Video 12). Figure 5(e) plots a pseudo-ECG showing this transition, which is also caused by the slow change of $[\mathrm{Na}^+]_\mathrm{i}$ (right panel).

Finally, we carry out 2D tissue simulation using the modified HH model (see the Appendix) used in our previous study [30] to demonstrate that bistable spiral waves can also occur in neural tissue (Fig. 6; Videos 13 and 14). Similar spiral wave dynamics (chaotic meandering) occur at the fast to slow spiral wave transition [up arrow in Fig. 6(d)] as in cardiac tissue [Figs. 2(c) and 2(d)] due to fast and slow wave interaction. The transition occurs at a larger G_Na in 2D tissue [Fig. 6(d)] than in 1D cable [Fig. 6(c)] due to CV restitution and curvature effects. For the same reason, the slow to fast spiral wave transition (down arrow) also occurs at a larger G_Na.

IV. DISCUSSION AND CONCLUSIONS

Bistable spiral waves have been shown in simulations of generic excitable media using simple models [21–23], such as the FHN or FHN-type models, however, the bistable spiral waves have not been demonstrated experimentally in generic excitable media. On the other hand, in previous studies [25,26], we showed another type of bistable spiral wave behavior that can occur in cardiac tissue, in which $I_{\mathrm{Ca},L}$-mediated spiral wave and I_Na-mediated spiral wave can occur in the same tissue under the condition of long QT syndrome or in the presence of early afterdepolarizations. Experimental evidence of this bistable behavior has been demonstrated in these studies. In this study, we demonstrate a different bistable behavior in planar and spiral wave conduction in cardiac and neural tissue models. The mechanism of bistability is caused by a positive feedback loop between I_Na inactivation and wave-front ramp-up speed as detailed in our previous study on nerve conduction [30]. For bistable conduction to occur, the major requirement was speeding up of I_Na kinetics. In the simulations of this study, although we need to alter several parameters in each model (see the Appendix) to observe the bistable behaviors, the common changes are speeding up of the I_Na inactivation kinetics and lowering of the I_{K1} conductance. Speeding up I_Na inactivation facilitates the positive feedback loop for bistability and lowering I_{K1} conductance enhances excitability to facilitate conduction. In cardiac systems, I_Na mutations in Brugada syndrome and I_Na blocking drugs may speed up I_Na inactivation kinetics (see Table 1 in Ref. [40]). Drugs may block I_{K1}, such as synthetic opioids [41]. Therefore, the condition for bistable conduction can be satisfied under diseased conditions or under drugs in real cardiac systems. As we have shown in our previous study [30], this condition can be satisfied in neural systems. Therefore, this bistable planar or spiral wave conduction mechanism may be widely applicable to electrically excitable media.

Spiral waves as a mechanism of cardiac arrhythmias have been well accepted. It is thought that different spiral waves may correspond to different forms of arrhythmias

[14,20,42–44]. For example, a stable spiral wave gives rise to monomorphic ventricular tachycardia, a meandering spiral wave gives rise to polymorphic ventricular tachycardia, and spiral wave breakup results in ventricular fibrillation. Electrocardiogram recordings from clinical settings and experiments [45–53] have shown that transitions among different types of arrhythmias occur frequently, and some occur suddenly. It is not clear how these transitions occur, and the current thought is that the transitions correspond to the transitions among different types of spiral waves as well as focal excitations. However, how the transition from one type to another type of spiral wave occurs is not well understood, especially when it occurs suddenly. As discussed in our previous studies [25,26], bistable spiral waves or reentry can be a candidate mechanism for the transitions in arrhythmias, such as the transition from Torsade de Pointes to ventricular fibrillation. As shown in Fig. 5 in this study, slow ion accumulation can convert one type to another type of spiral wave dynamics by slowly moving the system to the saddle-node bifurcation, and the transitions occur suddenly. These transitions can be candidate mechanisms for the transitions widely seen in cardiac arrhythmias [45–53], as well as in neural diseases [54,55].

In conclusion, a positive feedback loop between I_{Na} inactivation and wave-front ramp-up speed can form and cause a saddle-node bifurcation to result in bistable planar and spiral waves in electrically excitable media, such as cardiac and neural fiber and tissue, in which both slow and fast waves are triggered by different stimulation protocols. Moreover, the two types of spiral wave conduction may interact to give rise to more complex spiral wave dynamics. The transitions between different spiral wave behaviors via saddle-node bifurcation can be a candidate mechanism for transitions widely seen in cardiac arrhythmias and neural diseases.

ACKNOWLEDGMENTS

This work was supported by National Institutes of Health Grants No. R01 HL134709, No. R01 HL139829, No. R01 HL157116, and No. P01 HL164311. Z.Z. was supported by the National Natural Science Foundation of China under Grants No. 12375033, No. 11975131, and No. 12235007, Zhejiang Provincial Natural Science Foundation of China under Grant No. LY23A050002, and K. C. Wong Magna Fund at Ningbo University. Y.Z. was supported by the Graduate Student Scientific Research and Innovation Project of Ningbo University.

APPENDIX: MODIFICATIONS TO THE ACTION POTENTIAL MODELS

1. Modifications to the LR1 model

To simulate bistable conduction and spiral wave dynamics, we modify the LR1 model in this study. Here we give a brief description of the differential equations of the original LR1 model [33] and our modifications.

The membrane voltage V is described by the following differential equation:

$$\frac{dV}{dt} = -(I_{\mathrm{ion}} + I_{\mathrm{sti}})/C_m, \tag{A1}$$

where $C_{\mathrm{m}} = 1\mu\mathrm{F/cm}^2$ is the membrane capacitance. I_{sti} is the stimulus current density. I_{ion} is the total ionic current density consisting of different types of ionic currents, i.e.,

$$I_{\mathrm{ion}} = I_{\mathrm{Na}} + I_{\mathrm{si}} + I_K + I_{K1} + I_{Kp} + I_b, \tag{A2}$$

where I_{Na} is the Na^+ current. I_{si} is called the slow inward current, which is known as the L-type Ca^{2+} current ($I_{\mathrm{Ca},L}$). I_K, I_{K1}, and I_{Kp} are potassium (K^+) currents; I_b is the background current. I_{K1}, I_{Kp}, and I_b are functions of voltage. I_{Na}, I_{si}, and I_K are functions of voltage and gating variables, with the following formulations:

$$I_{\mathrm{Na}} = G_{\mathrm{Na}} m^3 h j (V - E_{\mathrm{Na}}), \tag{A3}$$

$$I_{\mathrm{si}} = G_{\mathrm{si}} d f (V - E_{\mathrm{si}}), \tag{A4}$$

$$I_K = G_K X X_i (V - E_K), \tag{A5}$$

where m, h, j, d, f, and X are gating variables described by the following type of differential equation:

$$\frac{dy}{dt} = [y_\infty(V) - y)]/\tau_y(V), \tag{A6}$$

where y_∞ and τ_y are functions of V. We set $E_{\mathrm{si}} = 80$ mV and thus the differential equation for $[\mathrm{Ca}^{2+}]_{\mathrm{i}}$ was dropped since it becomes independent. Therefore, the model becomes a seven-variable model.

We multiply a factor γ to a conductance or time constant to change the parameter. For example, for the time constants τ_y, we multiply a prefactor $\gamma(\tau_y)$, i.e.,

$$\tau_y(V) \to \gamma(\tau_y) \times \tau_y(V). \tag{A7}$$

We change the following time constants: $\gamma(\tau_h) = 0.3$; $\gamma(\tau_d) = 0.3$; and $\gamma(\tau_f) = 0.5$. We also change the conductances from the original values to $G_{\mathrm{si}} = 0.12\ \mathrm{mS/cm}^2$, $G_K = 0.5\ \mathrm{mS/cm}^2$, and $G_{K1} = 0.2\ \mathrm{mS/cm}^2$. We vary G_{Na} for bistability but set the default value as $G_{\mathrm{Na}} = 9\ \mathrm{mS/cm}^2$.

2. Modifications to the physiologically detailed action potential models

We simulate tissue models with three physiologically detailed action potential models: the LRd model [34], the TP04 model [35], and the ORd model [36]. For these models, we make fold changes to both conductances and time constants as listed in Table I.

3. Modified HH model

For the modified HH model, the total ionic current density I_{ion} is

$$I_{\mathrm{ion}} = I_{\mathrm{Na}} + I_{\mathrm{Ca}} + I_K + I_L. \tag{A8}$$

In Eq. (A8), I_{Na} is the Na^+ current density described by $I_{\mathrm{Na}} = G_{\mathrm{Na}} m^3 h (V - E_{\mathrm{Na}})$. I_K is the K^+ current density described by $I_K = G_K n^4 (V - E_K)$. I_L is the leak current density described by $I_L = G_L (V - E_L)$. I_{Ca} is the Ca^{2+} current density described by $I_{\mathrm{Ca}} = G_{\mathrm{Ca}} d^2 f (V - E_{\mathrm{Ca}})$. This formulation is adopted from Medlock *et al.* [56] with addition of an inactivation gate f. m, h, n, d, and f are gating variables which are described by the

TABLE I. Fold changes of selected conductances and time constants for the three models. d_∞-shift is the voltage shift of d_∞ for the d gate. Blank means no change. Although different changes are made for bistability to occur in different models, the common changes are speedup of I_{Na} inactivation [reduction of τ_h, i.e., $\gamma(\tau_h) < 1$] and reduction of G_{K1}.

	LRd	TP04	ORd
$\gamma(G_{\mathrm{Na}})$	0.72	0.76	0.69
$\gamma(G_{\mathrm{Ca},L})$	0.62	0.65	0.52
$\gamma(G_{K1})$	0.3	0.1	0.03
$\gamma(G_{Ks})$	0.5		0.8
$\gamma(\tau_h)$	0.2	0.15	0.2
$\gamma(\tau_d)$			0.3
$\gamma(\tau_f)$		0.5	
$\gamma(\tau_j)$		0.3	
$\gamma(\tau_X)$	0.5		0.5
d_∞-shift			−10 mV

same differential equations as Eq. (A6) with $y_\infty = \frac{\alpha_y}{\alpha_y+\beta_y}$ and $\tau_y = \frac{1}{\alpha_y+\beta_y}$. α_y and β_y are rate constants that are functions of V and listed in Table II.

To observe bistable conduction, we make modifications to the original HH kinetics. We shift the kinetics (see Table II) to give rise to a resting potential of around −65 mV (the measured resting potential in *Aglantha digitale* is close to this value [31]). Some of the shifts are required for facilitating bistable conduction.

TABLE II. Changes of parameters from the original HH model. α_m and β_m are shifted 60 mV toward more negative voltages. α_h and β_h are shifted 75 mV toward more negative voltages. α_n and β_n are shifted 25 mV toward more negative voltages. E_{Na} and E_K are shifted 65 mV toward more negative voltages, and E_L is shifted 75.6 mV. The shifts are to change the resting potential from around zero in the original HH model to −65 mV and to facilitate bistable conduction.

	Original HH model	Modified HH model
α_m	$0.1\,\frac{25-\mathrm{V}}{\exp(\frac{25-\mathrm{V}}{10})-1}$	$0.1\,\frac{-35-\mathrm{V}}{\exp(\frac{-35-\mathrm{V}}{10})-1}$
β_m	$4\exp(\frac{-\mathrm{V}}{18})$	$4\exp(\frac{-60-\mathrm{V}}{18})$
α_h	$0.07\exp(\frac{-\mathrm{V}}{20})$	$0.07\exp(\frac{-75-\mathrm{V}}{20})$
β_h	$\frac{1}{\exp(\frac{30-\mathrm{V}}{10})+1}$	$\frac{1}{\exp(\frac{-45-\mathrm{V}}{10})+1}$
α_n	$0.01\,\frac{10-\mathrm{V}}{\exp(\frac{10-\mathrm{V}}{10})-1}$	$0.01\,\frac{-15-\mathrm{V}}{\exp(\frac{-15-\mathrm{V}}{10})-1}$
β_n	$0.125\exp(\frac{-\mathrm{V}}{80})$	$0.125\exp(\frac{-25-\mathrm{V}}{80})$
E_{Na}	120 mV	55 mV
E_K	−12 mV	−77 mV
E_L	10.6 mV	−65 mV

For d_∞ and f_∞, we use the following formulations: $d_\infty = \frac{1}{1+\exp(-\frac{\mathrm{V}+14}{k_d})}$ and $f_\infty = \frac{1}{1+\exp(\frac{\mathrm{V}+44}{k_f})}$. τ_d and τ_f are set as constants independent of V.

The parameters are set as $G_{\mathrm{Na}} = 75$ mS/cm^2, $G_{\mathrm{Ca}} = 3$ mS/cm^2, $G_K = 36$ mS/cm^2, $G_L = 0.3$ mS/cm^2, $\gamma(\tau_m) = 0.2$; $\gamma(\tau_h) = 0.35$, $\gamma(\tau_n) = 3$; $E_{\mathrm{Ca}} = 120$ mV; $\tau_d = 3$ ms, $\tau_f = 20$ ms, $k_d = 5.8$, and $k_f = 6$.

[1] A. T. Winfree, *The Geometry of Biological Time* (Springer, New York, 2001).

[2] P. Ball, *The Self-Made Tapestry: Pattern Formation in Nature* (Oxford University Press, Oxford, 1999).

[3] A. T. Winfree, Spiral waves of chemical activity, Science **175**, 634 (1972).

[4] O. Steinbock, V. Zykov, and S. C. Muller, Control of spiral wave dynamics in active media by periodic modulation of excitability, Nature (London) **366**, 322 (1993).

[5] G. Li, Q. Ouyang, V. Petrov, and H. L. Swinney, Transition from simple rotating chemical spirals to meandering and traveling spirals, Phys. Rev. Lett. **77**, 2105 (1996).

[6] B. N. Vasiev, P. Hogeweg, and A. V. Panfilov, Simulation of Dictyostelium Discoideum aggregation via reaction-diffusion model, Phys. Rev. Lett. **73**, 3173 (1994).

[7] M. Falcke and H. Levine, Pattern selection by gene expression in dictyostelium discoideum, Phys. Rev. Lett. **80**, 3875 (1998).

[8] D. Dormann, J.-Y. Kim, P. N. Devreotes, and C. J. Weijer, cAMP receptor affinity controls wave dynamics, geometry and morphogenesis in Dictyostelium, J. Cell. Sci. **114**, 2513 (2001).

[9] J. Lechleiter, S. Girard, E. Peralta, and D. Clapham, Spiral calcium wave propagation and annihilation in Xenopus laevis oocytes, Science **252**, 123 (1991).

[10] M. Falcke, M. Or-Guil, and M. Bar, Dispersion gap and localized spiral waves in a model for intracellular Ca^{2+} dynamics, Phys. Rev. Lett. **84**, 4753 (2000).

[11] X. Huang, W. C. Troy, Q. Yang, H. Ma, C. R. Laing, S. J. Schiff, and J. Y. Wu, Spiral waves in disinhibited mammalian neocortex, J. Neurosci. **24**, 9897 (2004).

[12] S. J. Schiff, X. Huang, and J. Y. Wu, Dynamical evolution of spatiotemporal patterns in mammalian middle cortex, Phys. Rev. Lett. **98**, 178102 (2007).

[13] J. M. Davidenko, A. M. Pertsov, R. Salomonsz, W. Baxter, and J. Jalife, Stationary and drifting spiral waves of excitation in isolated cardiac muscle, Nature (London) **355**, 349 (1992).

[14] R. A. Gray, J. Jalife, A. V. Panfilov, W. T. Baxter, C. Cabo, J. M. Davidenko, A. M. Pertsov, and A. T. Winfree, Mechanisms of cardiac fibrillation, Science **270**, 1222 (1995).

[15] A. Karma, Meandering transition in two-dimensional excitable media, Phys. Rev. Lett. **65**, 2824 (1990).

[16] D. Barkley, Linear stability analysis of rotating spiral waves in excitable media, Phys. Rev. Lett. **68**, 2090 (1992).

[17] A. T. Winfree, Varieties of spiral wave behavior: An experimentalist's approach to the theory of excitable media, Chaos **1**, 303 (1991).

[18] Z. Qu, F. Xie, A. Garfinkel, and J. N. Weiss, Origins of spiral wave meander and breakup in a two-dimensional cardiac tissue model, Ann. Biomed. Eng. **28**, 755 (2000).

[19] F. H. Fenton, E. M. Cherry, H. M. Hastings, and S. J. Evans, Multiple mechanisms of spiral wave breakup in a model of cardiac electrical activity, Chaos **12**, 852 (2002).

[20] Z. Qu, G. Hu, A. Garfinkel, and J. N. Weiss, Nonlinear and stochastic dynamics in the heart, Phys. Rep. **543**, 61 (2014).

[21] A. T. Winfree, Alternative stable rotors in an excitable medium, Phys. D (Amsterdam, Neth.) **49**, 125 (1991).

[22] H. Ito and L. Glass, Spiral breakup in a new model of discrete excitable media, Phys. Rev. Lett. **66**, 671 (1991).
[23] V. S. Zykov and E. Bodenschatz, Spiral waves within a bistability parameter region of an excitable medium, New J. Phys. **24**, 013036 (2022).
[24] J. Rinzel and D. Terman, Propagation phenomena in a bistable reaction-diffusion system, SIAM J. Appl. Math. **42**, 1111 (1982).
[25] M. G. Chang, D. Sato, E. de Lange, J.-H. Lee, H. S. Karagueuzian, A. Garfinkel, J. N. Weiss, and Z. Qu, Bi-stable wave propagation and early afterdepolarization-mediated cardiac arrhythmias, Heart Rhythm **9**, 115 (2012).
[26] M. G. Chang, E. de Lange, G. Calmettes, A. Garfinkel, Z. Qu, and J. N. Weiss, Pro- and antiarrhythmic effects of ATP-sensitive potassium current activation on reentry during early afterdepolarization-mediated arrhythmias, Heart Rhythm **10**, 575 (2013).
[27] Z. Qu, L.-H. Xie, R. Olcese, H. S. Karagueuzian, P.-S. Chen, A. Garfinkel, and J. N. Weiss, Early afterdepolarizations in cardiac myocytes: Beyond reduced repolarization reserve, Cardiovasc. Res. **99**, 6 (2013).
[28] J. Rinzel and J. B. Keller, Traveling wave solutions of a nerve conduction equation, Biophys. J. **13**, 1313 (1973).
[29] J. P. Keener and J. Sneyd, *Mathematical Physiology* (Springer, New York, 1998).
[30] Z. Zhang and Z. Qu, Bistable nerve conduction, Biophys. J. **121**, 3499 (2022).
[31] G. O. Mackie and R. W. Meech, Separate sodium and calcium spikes in the same axon, Nature (London) **313**, 791 (1985).
[32] B. Hochner and M. E. Spira, Two distinct propagating regenerative potentials in a single ethanol-treated axon, Brain Res. **398**, 164 (1986).
[33] C. H. Luo and Y. Rudy, A model of the ventricular cardiac action potential: Depolarization, repolarization, and their interaction, Circ. Res. **68**, 1501 (1991).
[34] C. H. Luo and Y. Rudy, A dynamical model of the cardiac ventricular action potential: I. simulations of ionic currents and concentration changes, Circ. Res. **74**, 1071 (1994).
[35] K. H. ten Tusscher, D. Noble, P. J. Noble, and A. V. Panfilov, A model for human ventricular tissue, Am. J. Physiol. Heart Circ. Physiol. **286**, H1573 (2004).
[36] T. O'Hara, L. Virag, A. Varro, and Y. Rudy, Simulation of the undiseased human cardiac ventricular action potential: Model formulation and experimental validation, PLoS Comput. Biol. **7**, e1002061 (2011).
[37] See Supplemental Material at http://link.aps.org/supplemental/10.1103/PhysRevE.108.064405 for videos accompanying this work.
[38] Z. Qu, J. N. Weiss, and A. Garfinkel, Cardiac electrical restitution properties and the stability of reentrant spiral waves: A simulation study, Am. J. Physiol. **276**, H269 (1999).
[39] Z. Zhang and Z. Qu, Life and death saddles in the heart, Phys. Rev. E **103**, 062406 (2021).
[40] Z. Zhang, P. Brugada, J. N. Weiss, and Z. Qu, Phase 2 re-entry without I_{to}: Role of sodium channel kinetics in Brugada syndrome arrhythmias, JACC: Clin. Electrophysiol. (2023).
[41] M. G. Klein *et al.*, Methadone blockade of cardiac inward rectifier K+ current augments membrane instability and amplifies U waves on surface ECGs: A translational study, J. Am. Heart Assoc. **11**, e023482 (2022).
[42] R. A. Gray, J. Jalife, A. V. Panfilov, W. T. Baxter, C. Cabo, J. M. Davidenko, and A. M. Pertsov, Nonstationary vortexlike reentrant activity as a mechanism of polymorphic ventricular tachycardia in the isolated rabbit heart, Circulation **91**, 2454 (1995).
[43] A. Garfinkel and Z. Qu, in *Cardiac Electrophysiology: From Cell to Bedside*, edited by D. P. Zipes and J. Jalife, (W.B. Saunders, Philadelphia, 1999), pp. 315–320.
[44] A. V. Panfilov, Spiral breakup as a model of ventricular fibrillation, Chaos **8**, 57 (1998).
[45] A. Leenhardt, E. Glaser, M. Burguera, M. Nürnberg, P. Maison-Blanche, and P. Coumel, Short-coupled variant of torsade de pointes. A new electrocardiographic entity in the spectrum of idiopathic ventricular tachyarrhythmias, Circulation **89**, 206 (1994).
[46] J. N. Weiss, A. Garfinkel, H. S. Karagueuzian, Z. Qu, and P. S. Chen, Chaos and the transition to ventricular fibrillation: A new approach to antiarrhythmic drug evaluation, Circulation **99**, 2819 (1999).
[47] S. G. Priori and C. Napolitano, Cardiac and skeletal muscle disorders caused by mutations in the intracellular Ca2+ release channels, J. Clin. Invest. **115**, 2033 (2005).
[48] F. Fenton, A. Karma, H. Hastings, and S. Evans, Transition from ventricular tachycardia to ventricular fibrillation as function of tissue characteristics computer model, Proc. 22nd Ann. Int. Conf. IEEE Eng. Med. Biol. Soc. **1**, 391 (2000).
[49] M. T. Keating and M. C. Sanguinetti, Molecular and cellular mechanisms of cardiac arrhythmias, Cell **104**, 569 (2001).
[50] Y.-R. Chen, F.-F. Yi, X.-Y. Li, C.-Y. Wang, L. Chen, X.-C. Yang, P.-X. Su, and J. Cai, Resveratrol attenuates ventricular arrhythmias and improves the long-term survival in rats with myocardial infarction, Cardiovasc. Drugs Ther. **22**, 479 (2008).
[51] E. Ferraro, L. Pozhidaeva, D. S. Pitcher, C. Mansfield, J. H. B. Koh, C. Williamson, O. Aslanidi, J. Gorelik, and F. S. Ng, Prolonged ursodeoxycholic acid administration reduces acute ischaemia-induced arrhythmias in adult rat hearts, Sci. Rep. **10**, 15284 (2020).
[52] C. Maniotis, D. G. Tsalikakis, A. T. Tzallas, V. Varnavas, K. Kontaras, C. Glava, G. G. Baltogiannis, A. Papalois, T. M. Kolettis, and Z. S. Kyriakides, Chronic skeletal muscle ischemia in rats decreases the inducibility of ventricular tachyarrhythmias after myocardial infarction, In Vivo **25**, 781 (2011).
[53] P. S. Chen, T. J. Wu, C. T. Ting, H. S. Karagueuzian, A. Garfinkel, S. F. Lin, and J. N. Weiss, A tale of two fibrillations, Circulation **108**, 2298 (2003).
[54] V. K. Jirsa, W. C. Stacey, P. P. Quilichini, A. I. Ivanov, and C. Bernard, On the nature of seizure dynamics, Brain **137**, 2210 (2014).
[55] P. Jiruska, M. de Curtis, J. G. R. Jefferys, C. A. Schevon, S. J. Schiff, and K. Schindler, Synchronization and desynchronization in epilepsy: Controversies and hypotheses, J. Physiol. **591**, 787 (2013).
[56] L. Medlock, L. Shute, M. Fry, D. Standage, and A. V. Ferguson, Ionic mechanisms underlying tonic and burst firing behavior in subfornical organ neurons: A combined experimental and modeling study, J. Neurophysiol. **120**, 2269 (2018).